

Chapter 9

Residual Stress Evaluation in Vitreous Enameled Steel Sheets by Digital Images Analysis of Microstructures

Rita Ambu, Andrea Zucchelli and Giangiacomo Minak

Abstract Composite vitreous-enameled steel sheet have become more attractive for structural applications. In this chapter, an investigation on the residual stresses, introduced during the manufacturing of these materials, is reported. The local structure evidences the presence of bubbles in the coating and the interface domain between the substrate and the external layer made of a complex material system where the ceramic and the metal constituents are mixed. This particular local structure can affect the distribution and entity of the residual stresses. Digital images of cross-section micrographs have been processed and used to discretize the material microstructure into a mesh suitable for finite element analysis. The residual stresses have been evaluated on coatings manufactured with different technologies and, in particular, the effect of the presence of bubbles on the stresses has been highlighted.

Keywords Vitreous enamel coating · Residual stress · Image processing · Finite element method

9.1 Introduction

Composite vitreous-enameled steel sheets are a special class of metal-ceramic composite materials obtained by a two stages coating process: the deposition of the enamel raw material over the metal surface and the firing at high temperature of

R. Ambu (✉)
University of Cagliari, Piazza d'Armi, 09123 Cagliari, Italy
e-mail: ambu@unica.it

A. Zucchelli · G. Minak
University of Bologna, Viale Risorgimento 2, 40136 Bologna, Italy
e-mail: a.zucchelli@unibo.it

G. Minak
e-mail: giangiacomo.minak@unibo.it

the metal-enamel system. A wide spectrum of industrial and domestic applications currently make use of these coatings (e.g., the treatment of components for household use, the protection of interior walls of reactors for chemical processes, the protection of mechanical components of rotary heat exchangers, and aircraft turbojets). Enameled steel components are appreciated for their esthetic properties as well as for their chemical characteristics. In particular, enameling of metal substrates is used to provide protection against chemical corrosion for applications in hostile environments such as in reactors for chemical processes. In fact, from a functional point of view, vitreous enamel coatings have an excellent resistance to chemical corrosion processes [1–3]. Steel enameling is also used to obtain low roughness surfaces, having no fouling, and/or antimicrobial properties. Vitreous enamel coatings surfaces are also characterized by high values of hardness (up to 800 HV) giving to coated components a good resistance to tribological phenomena such as abrasive wear [4]. Compared to other coatings for metals, such as thermally sprayed ceramics, vitreous enamel coatings are characterized by a chemical and not only a physical adhesion to the substrate achieved by a graded interface that is developed during the coating firing process. Enameled steel components are also subjected to internal stresses. From a macroscopic point of view, these internal stresses contribute to prevent the instability of enameled steel plate when subjected to impact event [5]. But, the presence of residual stresses also affects the coating failure due to cracks onset and propagation, the spallation of the coating, the shape changes of the coated components and in general can influence the performance of the entire coated parts. Even if enameling is nowadays an industrial practice, some of the mechanical performances of enameled composites have not been studied and others are not completely understood. Based on this fact, the present work is intended to add an original contribution about one of the main physical and microstructural aspects that characterize the enamel coating: the residual stress and its relationship with the local characteristics of the enamel matrix.

Residual stresses are introduced in the enameled substrate during the manufacturing process. In fact, during the cooling to room temperature thermal mismatch stress develops due to the difference between the coefficients of thermal expansion (CTE) of the vitreous enamel material and the metal substrate. Different methods have been used to measure the residual stresses in coatings: mathematical modeling [6, 7], mechanical methods [8], and material removal techniques [9]. Each technique has certain advantages and limitations; their applicability is determined by such factors as shape, dimensions, materials of the coating and the substrate, knowledge of the constituents' properties and processing conditions. The experimental methods can be either destructive or non destructive, but all use a global approach to the evaluation of the residual stress. The computational models may be better tools to identify potential problems and decide what changes in the coating process are necessary to control the residual stresses. However, most models of residual stresses assume that coatings are homogeneous in structure and therefore cannot predict stress concentrations. But, for a more exhaustive mechanical characterization, the study of the local distribution of the residual

stress is an important task. In particular, the identification of regions of high stress level in the coating structure is of major concern. In fact, the configuration of the local structure of the material, such as the presence of bubbles or the existence of a transition zone between the two constituents of the material, can affect the local values of the stresses, thus promoting or delaying the onset of the fracture of the material in service. This can be accomplished by directly evaluating the residual stress on the real microstructure of the material, obtained from digital micrographs processed to this task. Digital image processing, widely used in many fields of sciences and engineering, has been applied in material sciences for quantitative description of complex material microstructures [10, 11] and, in particular, for stress investigation in thermal spray coatings [12, 13].

In this chapter, a procedure based on the analysis of digital images of enamel coatings has been applied to the measurement of thermal stresses. The approach considered uses the digital images filtered and converted into a graphical format to perform finite element simulations on the real local structure of the material. In this study, coatings manufactured with different technologies were considered. A preliminary characterization of the microstructures was performed by quantitative measurements on digital images. Then, the thermal stresses were evaluated taking into account F.E.M. discretization of the coating structure of growing complexity.

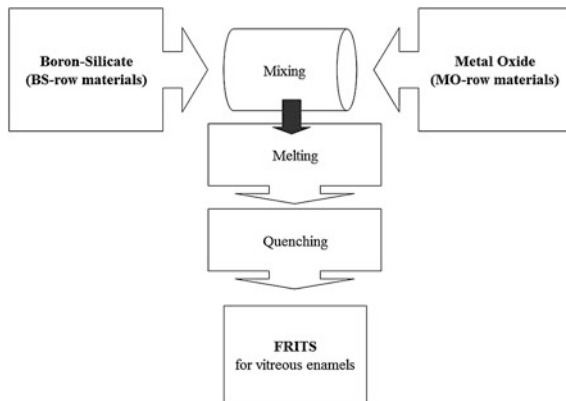
The results of the local approach were finally related to the characteristics of the microstructure.

9.2 Enamel Coating and Enameling Technology

Vitreous enamels are inorganic materials that are used as coatings for metallic components. These materials are based on a special ceramic-vitreous matrix in which specific additives are randomly dispersed. The ceramic-vitreous matrix is made by a mixture of various raw materials and elements and in particular it is based on boron-silicate glass added with metal oxides of titanium, zinc, tin, zirconia, alumina, etc. These additions are often used to enhance some important performances such as corrosion and wear resistance, mechanical strength, fracture toughness, and also esthetic functions. The compound obtained by mixing these rough materials is then fired at about 1,300 °C and quickly cooled into cold water, as shown in the scheme of Fig. 9.1. At the end of this process, the ceramic-vitreous matrix is obtained and it is commonly called frit.

In order to obtain the vitreous enamel raw materials, specific additives have to be mixed and milled with the frits. These additives are necessary to increase the adherence of the enamel to the metal substrate and also to give special properties and functions to the final coat. The mixing-milling process can be realized by a wet or a dry process. In the wet process, the vitreous enamel raw material consists on a slip in which the small grain of the frits and of the additives are homogeneously dispersed in water. In the case of the dry milling process, the addition of silicone oil enables the production of fine powder made by frits and additives

Fig. 9.1 Scheme of the frits for vitreous enamel raw material production



grains that can be applied to the metal substrate by an electrostatic deposition technology.

The wet enameling process consists of four phases shown in Fig. 9.2: (i) wet milling, (ii) wet spraying (or flow coating deposition), (iii) drying, and (iv) firing at high temperature (about 550 °C for low melting alloys, about 750 °C for cast iron and about 850 °C for steel). The dry process is based on three phases: (i) dry milling with silicone oil addition, (ii) electrostatic deposition, and (iii) firing at high temperature (about 550 °C for low melting alloys, about 750 °C in case of cast iron and about 850 °C for steel).

Figure 9.3 gives an example of the firing curve. This figure shows the typical firing diagram where the heating, the maturing, and the cooling phases are highlighted together with some photos of the enamel pellets over a metal substrate taken during the firing process. The photos of the pellets, taken with a heated microscope, show the enamel pellet transition from A up to B temperature during the firing phase, and the complete fusion of the enamel pellet during the maturing phase (C). It is interesting to note that during the cooling phase the enamel lens (D and E) does not change its shape and it consolidates over the metal surface.

During the firing process, the enamel raw material melts and interacts with the metal substrate, thus enabling the formation of a continuous varying structure.

As shown in the micrograph of the transversal section in Fig. 9.4, the interface zone between the substrate and the external layer is made of a complex material system where the vitreous enamel and the metal constituents are mixed. In particular, three main regions can be identified, starting from the bottom of Fig. 9.4a: a first region is made of metal, the second region is the interphase where both metal and enamel constituents are mixed, and the third region is composed by the vitreous enamel material. Referring to Fig. 9.4b, the presence of metallic dendrites that hinder the substrate and the external layer passing through the interphase region can also be noted.

As already mentioned in the introduction, the mechanical behavior of the vitreous enamel-metal composite at room temperature is greatly influenced by

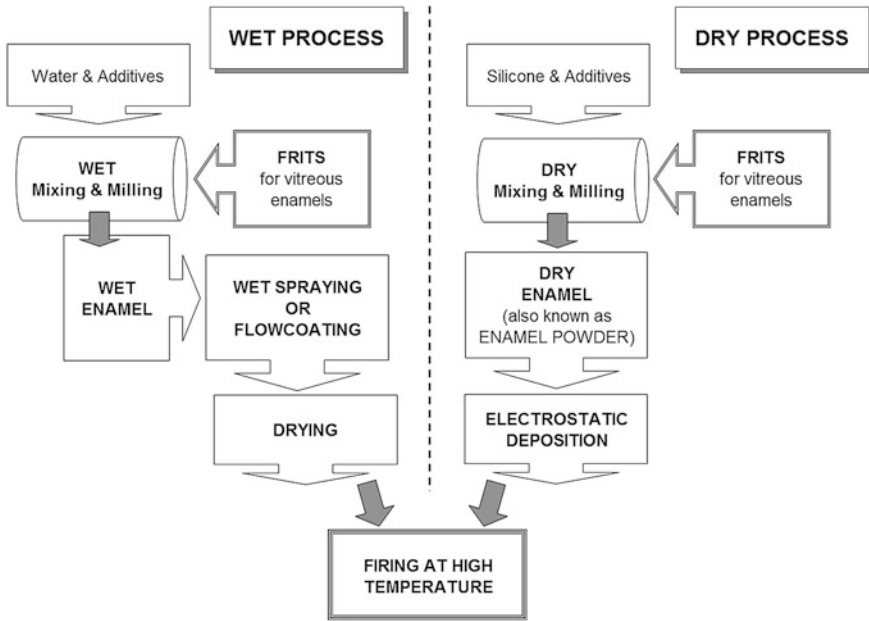


Fig. 9.2 Scheme of the enameling coating processes in the case of wet enamel or dry enamel deposition techniques

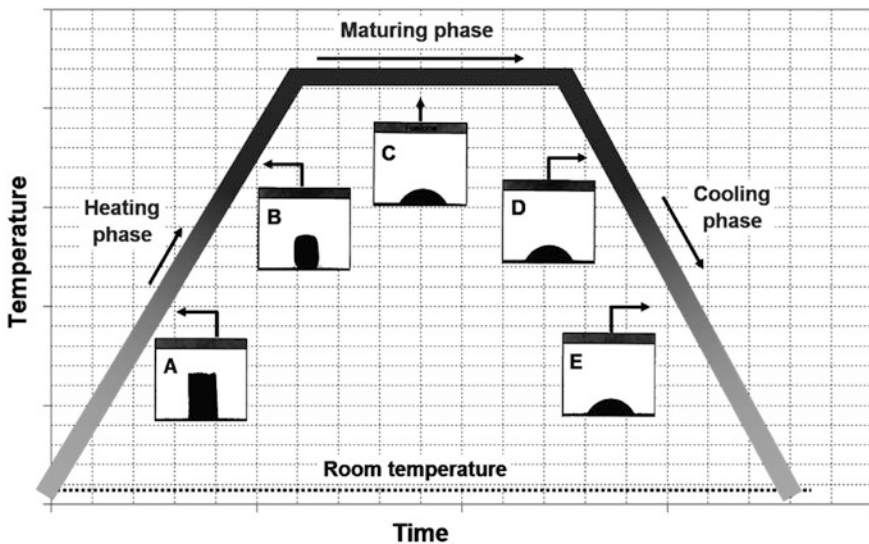


Fig. 9.3 Scheme of firing curve for the enamel-substrate system with details of the enamel transition during the thermal treatment

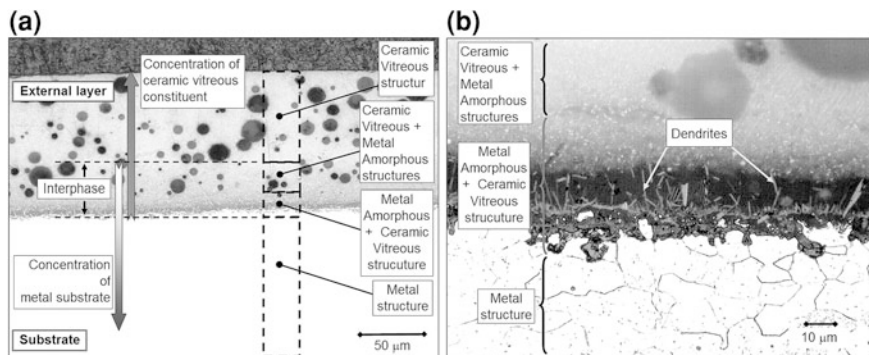


Fig. 9.4 Enamel-steel composite structure. **a** General micrograph view of the enamel and metal composite; **b** detail of the interface between the enamel coating and the metal substrate

internal stresses developed during the firing and cooling phases. In the firing of an enamel, the sealing at elevated temperatures is accomplished without excessive stress development because the enamel is relatively fluid at the firing temperatures and can easily assume the surface dimensions of the metal to which it is applied. Any difference in the contraction of the metal and the enamel is of little consequence until the temperature is reached at which the cooling rate is too rapid to allow flow of one on the other or internal flow in either. The stress initially developed is only a fraction of that which would be expected when considering the difference in the rates of contraction of metal and enamel. However, as cooling proceeds, the amount of flow decreases and the rate of stress development becomes a function of differential contraction rates, moduli of elasticity, thickness, and shape. To better understand this phenomenon, the expansion curves of both low carbon-steel and vitreous enamel have to be analyzed.

Referring to Fig. 9.5, it can be observed that although the metal has a straight-line thermal expansion relationship with temperature, the curve for enamel is not straight and undergo a radical change in direction at about the Break Rate Temperature (BRT), which is, in the case of enamel used in the present study, at about 400 °C. Therefore, enamel has a lower expansion coefficient than low-carbon-steel when temperature increases from room temperature. But when the break in the enamel curve is overcome, the enamel expansion rate increases becoming greater than the ones of the low-carbon-steel. During this expansion rate change, there is a small temperature range at which the enamel catches up on the average rate of expansion of the low-carbon-steel: the primary equivalent rate temperature, shown in Fig. 9.3. At the equivalent rate temperature, the rate of expansion of the enamel and the low-carbon-steel are alike, but the overall expansions at this point are different. Since the conditions of like expansion and contraction between the enamel and the low-carbon-steel may occur at other temperature when the enamel experiences crystallization, contains crystals which invert, or is subjected to special heat treatments, these others are called secondary equivalent rate temperatures, shown in Fig. 9.5. The enamel curves show a drop at F (enamel fusion

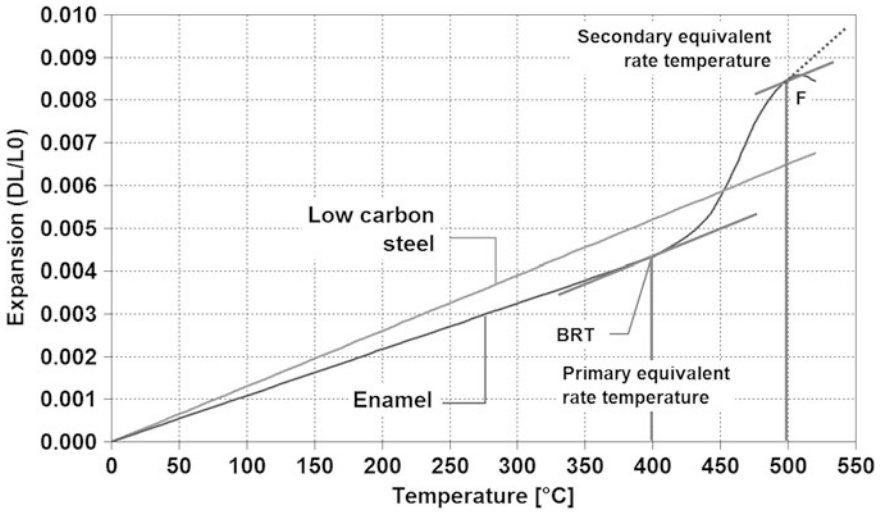


Fig. 9.5 Thermal expansion diagram of the low carbon steel and of the vitreous enamel material used in the present study

temperature) but this is a failure in the structural strength as the enamel actually continues to expand as indicated by the dotted line. Because of the high mobility of the enamel above this temperature, the stress and strain in enamel low-carbon-steel composite system become very low, even though they both continue to expand at different rates with increase in temperature. The flow of the enamel glass substantially relieves the stresses during the heating and cooling of the composite at temperatures above the BRT. The amount of tension in low-carbon-steel and compression in enamel would actually be a function of the contraction differences in cooling from BRT to room temperatures during the cooling phase. For a fixed component geometry, the intensity of residual stresses acting on the enameled steel composite can be pre-determined by means enamel design (compositions of frits and additions) aimed to match proper values of both BRT and coefficient of thermal expansion.

9.3 Materials and Characterization

Sheets of 0.8 mm thick of a very low carbon steel, as reported in Table 9.1, were coated by two blue enamels: one is a wet enamel prepared for the wet-spray application and the other one is a dry enamel for electrostatic deposition. Steel specimens have a rectangular shape: 250 mm in length and 40 mm in width.

Both enamel raw materials were prepared by the same types of frits whose compositions, given by the frits producer, are summarized in Table 9.2.

Table 9.1 Steel sheets chemical composition (%)

	Elements						
	C	Mn	Si	P	S	Al	Cu
wt%	0.003	0.31	0.03	0.025	0.04	0.025	0.032

Table 9.2 Composition of enamel frits in wt% of oxides

	Oxides											
	SiO ₂	B ₂ O ₃	Na ₂ O	K ₂ O	CaO	BaO	MnO	CoO	NiO	CuO	TiO ₂	Li ₂ O
Frit 1	58	10	12	3	3	4	2.6	2.8	2.4	1.2	1	–
Frit 2	69	4	10	4	–	–	2.8	2.2	–	–	13	5

The wet enamel was prepared by milling, in an alumina ball mills, the two frits with the proper additions of water, clay, and metal oxides for color control. The milling process takes 4 h in order to obtain wet blends containing particles of controlled size ($\sim 45 \pm 6 \mu\text{m}$). The steel sheets for the wet enamel deposition were pre-treated according to the following seven steps: (i) degreasing at 60 °C with alkaline degreasing bath, (ii) acid attack in a 5 vol% solution of sulfuric acid at 60 °C, (iii) room temperature water bath, (iv) nickel deposition by immersion in a 1.2 % of NiSO₄ bath, (v) room temperature water bath, (vi) immersion in a 0.3 % neutralizer solution at 60 °C, and (vii) drying up at 110 °C.

The dry enamel was prepared by milling, in an alumina ball mills, the two frits with the proper additions of silicone oil. The milling process takes 9 h in order to obtain a dry powder with a controlled size ($\sim 28 \pm 5 \mu\text{m}$). The steel sheets used to prepare the samples by the dry enamel raw material were polished to take out all superficial impurities due to sheets machining.

After enamels deposition over the steel substrates, the all systems enamel-substrate were fired at the same conditions:

- heating phase, from room temperature to 850 °C, in 6 min;
- maturing phase, at a constant temperature of 850 °C, for 6.5 min;
- cooling phase from 850 °C to room temperature in 7 min.

In Fig. 9.6, two examples of micrographics images of the transversal section of the enameled steel are reported.

In particular, in Fig. 9.6a the transversal section of the coating obtained by means of the wet enamel is reported, and in Fig. 9.6b the coating obtained by means of the dry enamel. From these images, it is possible to note that in the case of wet enamel the distribution of the bubbles in the coating section is almost uniform; on the contrary, in the case of the dry enamel the bubbles are dispersed near the external face of the coating. This fact is due to the raw material formulation and in particular to the presence of the clay in the wet enamel formulation. The usage of clays in the wet enamel manufacturing aims to control both the slips rheology as well as the bubbles distribution in the final coating. Moreover, in both images, it is possible to note the presence of dendrites between the coating and the substrate.

Fig. 9.6 Examples of enamel coating obtained by **a** wet enamel raw material and by **b** dry enamel raw material; in the case **(b)** the bubble segregation near the external coating face is highlighted by the *dashed line*

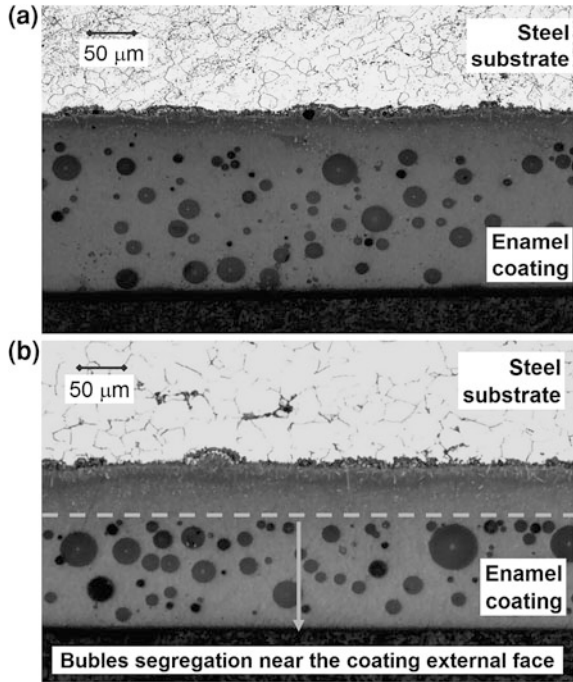


Table 9.3 Main characteristics of the coating microstructure

	Bubbles percentage		Bubbles diameter (μm)	
	M.V.	S.D.	M.V.	S.D.
Wet enamel	15	4	17	8
Dry enamel	17	6	15	6

In Table 9.3, the main microstructure characteristics of the enamel coatings are summarized. In particular, the bubbles density (also known as blistering) and the bubbles diameter are analyzed in terms of mean value and standard deviation.

The numerical analyses have been performed by considering the physical and the mechanical properties, respectively for the metal substrate and the enamel coating, summarized in Table 9.4.

In particular, the mechanical performance of low carbon steel was assessed by tensile tests according to UNI EN 10002. The mechanical properties of vitreous enamel material (E and ν) were estimated by four point bending tests [3]. The coefficient of thermal expansion of vitreous enamel material was determined by a heating dilatometer while the coefficient of thermal expansion for the metal was taken from the literature [1].

Table 9.4 Material properties

Material	α ($10^{-5} \text{ } ^\circ\text{C}^{-1}$)	BRT ^a ($^\circ\text{C}$)	E (MPa)	ν
Low carbon steel	1.35	–	180,000	0.3
Wet enamel	1.18	400	70,000	0.27
Dry enamel	1.23	400	70,000	0.27

^a The Break Rate Temperature (BRT), as mentioned in the Sect. 9.2, is the temperature below which, during the cooling phase, the residual stress starts developing

9.4 Methodology

The analysis of the residual stress was performed by means of the digital images of cross-section micrographs of the material. These images highlight the local characteristics of the material such as the bubbles and the graded interface between the two constituents.

In particular, the presence of bubbles in the coating is mostly evidenced, as can be observed in Fig. 9.7, where one of the analyzed images is reported.

The procedure followed for image analysis can be as summarized. A median filter (3×3) is first applied to the image [14, 15]. The next step consists in thresholding the image, so as to expose the geometries of interest. The threshold value is set with an iterative procedure based on the histogram image distribution. Morphological operations are then applied to the binarized image. In particular, closing was employed in order to fill in small holes, while opening was used for clustered pores.

The binary image obtained highlights the bubbles in the coating and the graded layer between the coating and the substrate as dark objects on a light background, as evidenced in Fig. 9.8.

The discretization of the coating requires the identification of the borders of the objects in the binary image. To highlight the sharp changes in intensity, an edge detection filter is applied to the image. For this task, a Sobel operator is used, based on convolving the image with a small, separable, and integer value filter in horizontal and vertical direction. The edge detection allows to produce an image where, in particular, the geometry and location of the characteristics of interest is well identified.

As known, the binary interface image uses the unit gray level to represent the interface pixels. The closed interfaces are a cluster of the pixels with the unit gray level. In order to carry out the mechanical analysis, finite element meshes must be generated for the material distribution and geometry shown in the refined binary image. The finite element meshes cannot be generated directly from the binary interface image. The discrete interface pixels have to be transformed into their geometry vector data format. This conversion is the preliminary procedure for automatic generation of the finite element meshes for the material.

Fig. 9.7 Image of the coating

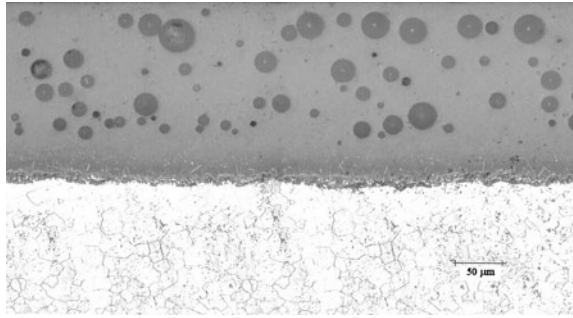


Fig. 9.8 Binarized image of the coating

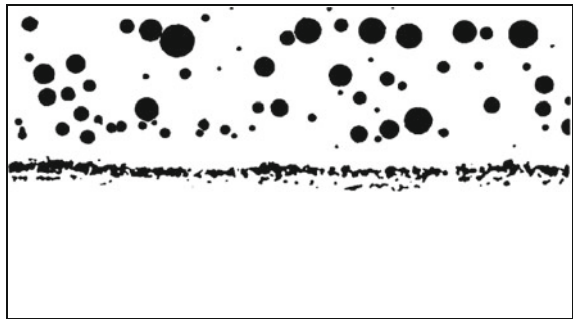
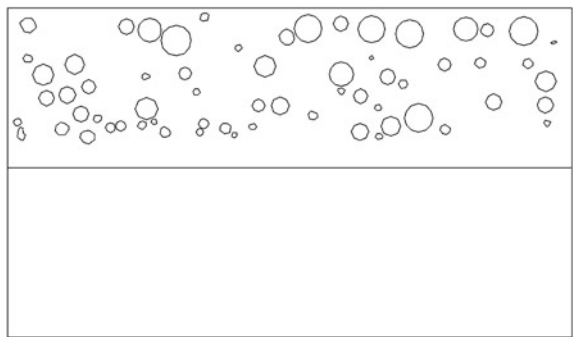


Fig. 9.9 Vectorized image of the coating



Once performed the image conversion, a scale transformation is applied to the image in the graphical format, according to the calibration data. The image magnification is 1,680 pixel/mm. The result finally obtained is reported in Fig. 9.9.

It has to be observed that in Fig. 9.9, the graded layer between the coating and the metal substrate has been disregarded.

The discretization of the zone with the graded layer between the coating and the metal substrate required a further analysis. In fact, as previously discussed, the structure of the graded layer is very complex, also if the extension can be estimated from filtered images of high magnification such as that reported in Fig. 9.10 together with a brightness diagram along with a line.

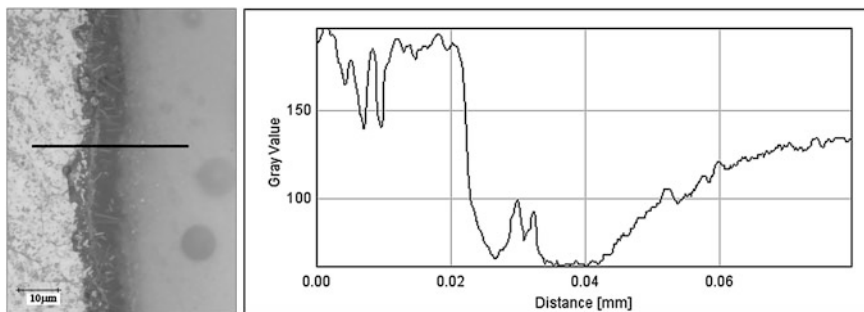


Fig. 9.10 The interface between the coating and substrate

Consequently, it is difficult to obtain a discretization of this zone of the material on which a representative finite element mesh should be generated. The finite element meshes directly obtained from the binarized images were not satisfactory, in particular because a dense discretization was obtained and was difficult to associate the proper mechanical and thermal properties in the interface zone.

To further investigate on this zone of the material, energy dispersive X-ray (EDX) analysis was used to study the composition and microstructural changes occurring near the coating-substrate interface. The results are reported in Fig. 9.11.

The diagrams show the reciprocal interaction between the coating and the steel substrate. In fact, starting from the inner substrate, steel slowly degrades into the coating components, while the percentage of silicate, basic component of the coating, asymptotically grows from the surface of the substrate.

Finally, a simplified discretization was adopted. The graded layer was simulated by introducing graded interlayers, as reported in literature for the numerical simulation of two dissimilar materials joined by a graded layer [16], with intermediate mechanical and thermal properties between those of the coating and the substrate. This discretization also gives the capability to separately evaluate the influence on the residual stress of the bubbles in the coating and the presence of the graded layer.

9.5 Results and Discussion

The vectorized images were imported in a commercial finite element code to perform the analysis of the residual stress. The finite element simulations were performed by means of ANSYS F.E.M. software. The images of the coating microstructures were discretized with quadrilateral plane elements to create a finite-element mesh adapted to fit within material boundaries. The bubbles in the microstructure were considered to be empty cells whose interstices are free to move.

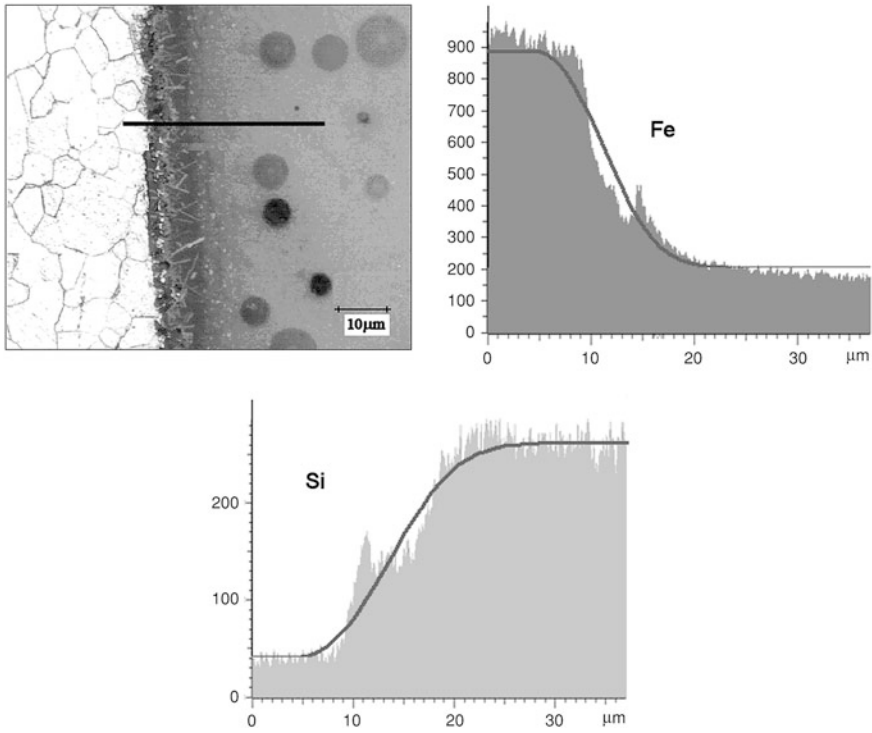


Fig. 9.11 EDX maps relative to the interface between the coating and substrate

Figure 9.12 reports a detail of the F.E.M. discretization relative to a micrograph analyzed in this study.

The analysis was performed by the simulation of the cooling of the material from the maximum temperature reached during the manufacturing to the room temperature, assuming a temperature gradient of 400 °C. In particular, micrographs of coatings representative of the two manufacturing processes before described have been considered. The thickness of the steel sheet introduced in each model is 0.8 mm. The first simulations did not take into account the presence of the graded layer, as discussed before.

Figure 9.13 shows the gray-scale map of the thermal stress for a coating manufactured with the wet enameling technique.

The figure reports the component of the residual stress in the longitudinal direction, indicated in the figure as x . As for the boundary conditions, a longitudinal length of the material three times that of the original image was considered in order to demonstrate the stress build-up in a wide spread coating.

The stress contours show a steep variation at the interface between the coating and the substrate, as also evidenced in the diagram of Fig. 9.14a where the thermal stress along with a vertical cross-section through the coating, in particular, relative

Fig. 9.12 A detail of the F.E.M. mesh

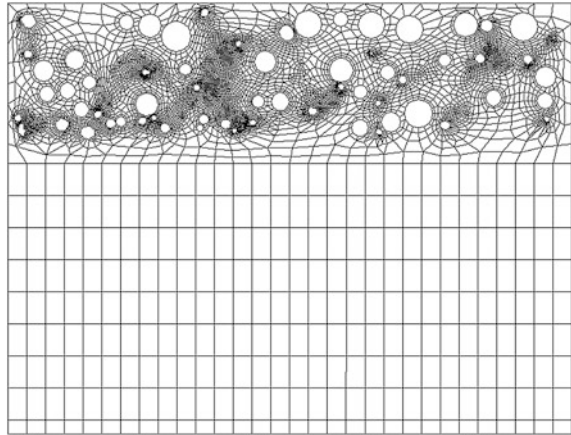
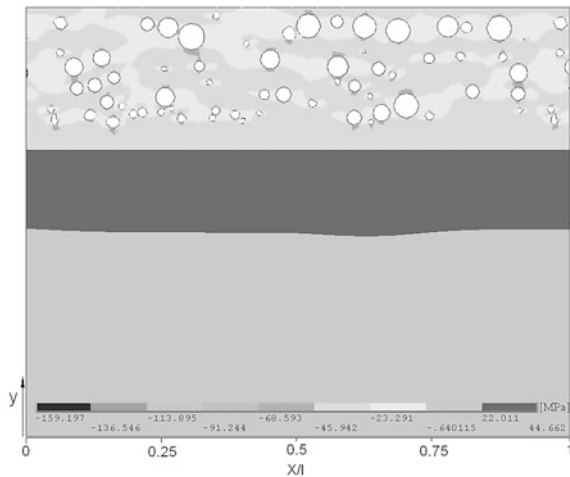


Fig. 9.13 Residual stress for a coating manufactured with wet enameling procedure



to $X/l = 0.5$, is reported. A zone of tension in the steel substrate and compression stress in the coating are also evidenced.

However, differently from an analogous theoretical coating devoid of bubbles, whose trend of the residual stress is also reported in the figure, higher values of stress exist in the real structure of the coating due to the bubbles. A detail of Fig. 9.13, reported in Fig. 9.14b, shows the zone where the maximum value of stress was measured in the coating.

A similar analysis was conducted on cross-section micrographs relative to the enameled coatings manufactured using the dry enameling technique.

Figure 9.15 reports the gray-scale map of the stress in the longitudinal direction obtained for a representative image.

It can be observed that the maximum values of the residual stress measured in the material are lower than those obtained for the coating produced with the wet

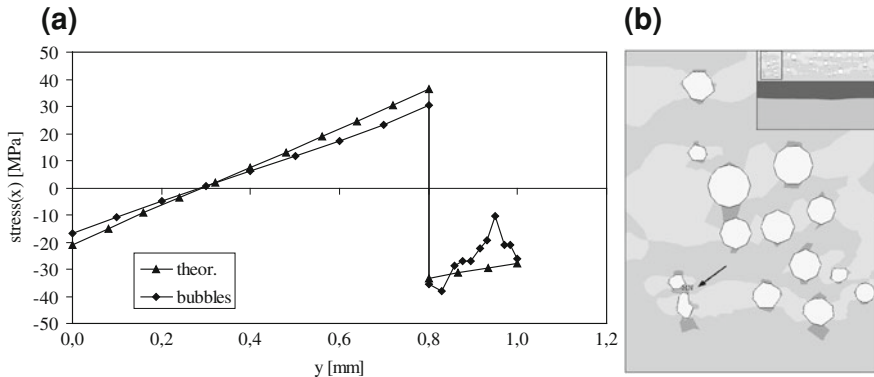
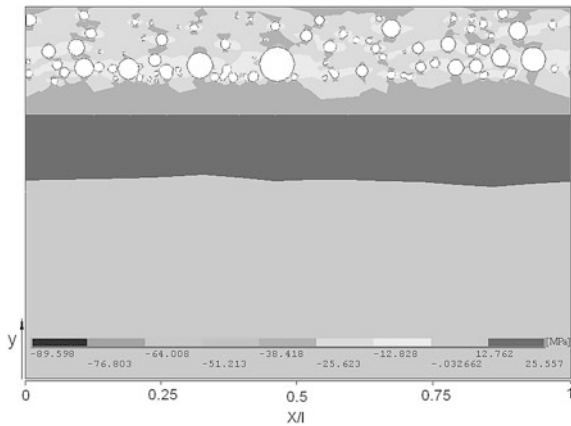


Fig. 9.14 The thermal stress in a wet enameling coating. **a** The stress along with a transversal section **b** a detail of the stress near the bubbles

Fig. 9.15 Residual stress for a coating manufactured with the dry enameling technique



enameling manufacture processing. It was expected, since a difference between the thermal expansion coefficient of the two coating systems exists.

Figure 9.16a reports the thermal stress along with a vertical cross-section through the coating, relative to $X/l = 0.5$, while in Fig. 9.16b a detail of Fig. 9.15 is shown, where the zone of the maximum stress measured in the coating is evidenced.

The trend of the stresses is similar to that reported for the previous coating analyzed, and the scattering of the values in the coating is noticeable with respect to the linear trend of a theoretical coating devoid of bubbles.

A further analysis was conducted by taking into account the graded layer between the coating and the substrate. The graded layer was introduced in the models by interposing two slight layers with a thickness of 0.010 mm and linearly variable mechanical and thermal properties between the two constituents. The thickness of the graded layer was derived from measurements on images of higher

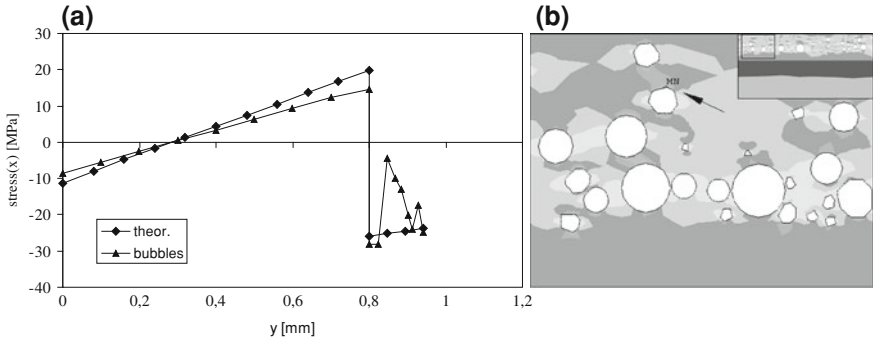
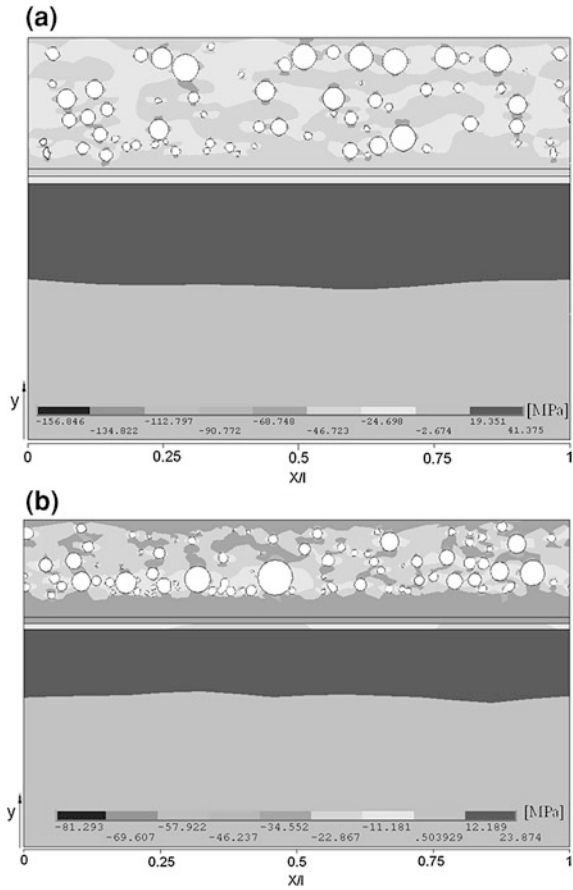


Fig. 9.16 The thermal stress in a dry enameling coating. **a** The stress along with a transversal section **b** a detail of the stress near the bubbles

Fig. 9.17 Residual stress for coatings with a graded layer. **a** Wet enameling technique and **b** dry enameling technique



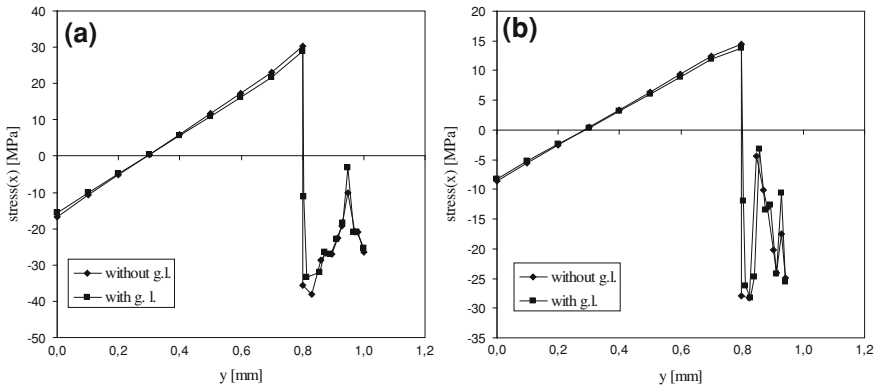


Fig. 9.18 The residual stress along with a transversal section. **a** Wet enameling technique and **b** dry enameling technique

magnification and the values were found similar for the coatings manufactured with the different technologies.

Figure 9.17 shows the gray-scale map of the longitudinal stress obtained in these simulations.

In particular, Fig. 9.17a is relative to the coating manufactured with the wet enameling technique, while Fig. 9.17b is relative to the coating manufactured with the dry enameling technique.

The results show that the presence of the graded layer gives a contribute to the reduction of the maximum values of the thermal stress in the coating, as compared with the previous simulations.

Figure 9.18 shows the trend of the residual stress along with a transversal section, corresponding to $X/l = 0.5$, relative respectively to the coatings manufactured with the two manufacturing technologies.

From the diagrams it can be observed, in particular, that the steep discontinuity in stress at the coating-substrate interface is slightly attenuated when the graded layer is introduced in the models. However, differently from the functionally graded materials where, typically, the graded interlayers are used to mitigate the thermal stresses [17], this occurrence is not particularly evidenced in the coatings analyzed. Among the different factors that contribute to this circumstance, such as geometry and composition, probably, the presence of the bubbles masks the effect on the residual stress of the graded interface between the coating and the substrate.

9.6 Conclusions

In this chapter, a method based on digital images of cross-section micrographs has been applied to the analysis of residual stress in enamelled coatings. The results, relative to coatings manufactured with different technologies, highlight the

relationship between the local characteristics of the structure and the stresses. In particular, the presence of bubbles in the coating seems to have a significant role on the distribution of the local residual stress while the effect of the graded layer between the coating and the substrate seems to be attenuated and this aspect will be further investigated.

References

1. Andrews, A.I.: Porcelain Enamel. The Garrard Press, Champaign (1961)
2. Vargin, V.V.: Technology of Enamels. Maclaren and Sons, London (1967)
3. Chelli, A., Poletti, R., Pignatti, L., Bruscoli, F., et al.: Composite enameled steel elements for air preheaters and gas-gas heaters: an integrated approach from sheet forming and enamelling to basket assembly. In: XXI International Congress on Porcelain Enamel, Shanghai, pp. 130–158, 18–22 May 2008
4. Chelli, A., Poletti, R., Pignatti, L., et al.: Experimental study of the mechanical and tribological properties of enameled steel plate, (abstract in english, full text in italian). *Smalto Porcellanato* **3**, 1–27 (2006)
5. Zucchelli, A., Minak, G., Ghelli, D.: Low-velocity impact behavior of vitreous-enameled steel plates. *Int. J. Impact Eng.* **37**, 673–684 (2010)
6. Zhang, X.C., Xu, B.S., Wang, H.D., et al.: An analytical model for predicting thermal residual stresses in multilayer coating systems. *Thin Solid Films* **488**, 274–282 (2005)
7. Bengtsson, P., Persson, C.: Modelled and measured residual stresses in plasma sprayed thermal barrier coatings. *Surf. Coat. Tech.* **92**, 78–86 (1997)
8. Swank, W.D., Gavalya, R.A., Wright, J.K., Wright, R.N.: Residual stress determination from a laser-based curvature measurement. INEEL/CON-99-01176. http://www.osti.gov/bridge/productbiblio.jsp?osti_id=758128(2000) Accessed 11 May 2009
9. Lima, C.R.C., Nin, J., Guilemany, J.M.: Evaluation of residual stresses of thermal barrier coatings with HVOF thermally sprayed bond coats using the Modified Layer Removal Method (MLRM). *Surf. Coat. Tech.* **200**, 5963–5972 (2006)
10. Wejrzanowski, T., Sychalsky, W.L., Rozniatowsky, K., et al.: Image based analysis of complex microstructures of engineering materials. *Int. J. Appl. Math. Comput. Sci.* **18**, 33–39 (2008)
11. Von Bradke, M., Gitzhofer, F., Henne, R.: Porosity determination of ceramic materials by digital image analysis—a critical evaluation. *Scanning* **27**, 132–135 (2005)
12. Ghafouri-Azar, R., Mostaghimi, J., Chandra, S.: Modeling development of residual stresses in thermal spray coatings. *Comput. Mater. Sci.* **35**, 13–26 (2006)
13. Wang, Z., Kulkarni, A., Deshpande, S., et al.: Effect of pores and interfaces on effective properties of plasma sprayed zirconia coatings. *Acta Mater.* **51**, 5319–5334 (2003)
14. Russ, J.C.: The image processing handbook. CRC Press, Boca Raton (1995)
15. Abramoff, M.D., Magelhaes, P.J., Ram, S.J.: Image Processing with Image. *J. Biophotonics Int.* **11**, 36–42 (2004)
16. Hsueh, C.H., Lee, C.S.: Modeling of elastic thermal stresses in two materials joined by a graded layer. *Compos. Part B-Eng.* **34**, 747–752 (2003)
17. Ravichandran, K.S.: Thermal residual stress in a functionally graded material system. *Mater. Sci. Eng. A-Struct.* **201**(269), 276 (1995)